Title

Selectively accessing the hotspots of optical nanoantennas by self-aligned dry laser ablation

Permalink

Journal

ISSN

Authors

Schäfer, Christian
Perera, Pradeep N
Laible, Florian
et al.

Publication Date

DOI

Peer reviewed

Selectively accessing the hotspots of optical nanoantennas by self-aligned dry laser ablation

Christian Schäfer,[a] Pradeep N. Perera,[b,c] Florian Laible,[a] Deirdre L. Olynick,[b,d] Adam M. Schwartzberg,[b] Alexander Weber-Bargioni,[b] Stefano Cabrini,[b] Peter J. Schuck,[b,e] Dieter P. Kern[a] and Monika Fleischer*[a]

Plasmonic nanostructures serve as optical antennas for concentrating the energy of incoming light in localized hotspots close to their surface. By positioning nanoemitters in the antenna hotspots, energy transfer is enabled, leading to novel hybrid antenna-emitter-systems, where the antenna can be used to manipulate the optical properties of the nano-objects. The challenge remains how to precisely position emitters within the hotspots. We report a self-aligned process based on dry laser ablation of a calixarene that enables the attachment of molecules within the electromagnetic hotspots at the tips of gold nanocones. Within the laser focus, the ablation threshold is exceeded in nanoscale volumes, leading to selective access of the hotspot areas. A first indication of the site-selective functionalization process is given by attaching fluorescently labelled proteins to the nanocones. In a second example, Raman-active molecules are selectively attached only to nanocones that were previously exposed in the laser focus, which is verified by surface enhanced Raman spectroscopy. Enabling selective functionalization is an important prerequisite e.g. for preparing single photon sources for quantum optical technologies, or multiplexed Raman sensing platforms.

Keywords: plasmonic nanostructure, hybrid antenna-emitter, self-alignment, laser ablation, nanocone, functionalization

Introduction

The ability of plasmonic nanostructures, or optical nanoantennas, to concentrate the energy of an incoming light wave in tiny controllable volumes, otherwise known as hotspots, has led to intense research and manifold applications. The presence of a nanoantenna results in a strongly enhanced local electric near-field and an increase in the local density of states. If nanoantennas are combined with individual nano-emitters (atomic, molecular or nano-crystalline emitters, e.g. fluorophores or quantum dots), the fundamental physics of the hybrid system changes significantly. Adding an antenna can lead to dramatic changes in the directivity of the emission and its polarization,[1-3] a distinct decrease in the lifetime,[4-8] the appearance of nonlinear optical effects such as higher-harmonic generation,[9,10] or strong fluorescence enhancement.[8] Surface and tip enhanced Raman spectroscopy (SERS and TERS) famously utilize the strongly confined fields near sharp tips or nanoparticles to enhance the signal from molecules by several orders or magnitude.[11-14] In any case, the energy transfer between the nanoantenna and emitter strongly depends on their distance and relative orientation. The more confined the field, the more critical the positioning of the nano-object, since minimal shifts translate into huge changes in interaction strength.[15] Maximum coupling can be achieved when the emitter is positioned directly in the antenna hotspot. Therefore, one of the biggest challenges in the field of hybrid plasmonic systems is finding ways to optimally position nano-emitters with nanometer precision. On the one hand, most nanofabrication techniques have an inherent uncertainty on the order of a few to few tens of nanometers, such that reproducible positioning with single-nanometer precision remains elusive. On the other hand, in most cases the location of the hotspots is predicted from simulations. These however typically assume a perfect antenna shape, whereas the true hotspot location strongly depends on the exact nanoscale morphology of the fabricated structures.[16]

Creating hybrid nanoantenna-emitter-structures that contain only one to few nano-objects within the hotspots, and no further nano-object in the antenna's vicinity, has direct relevance for major research directions. From a fundamental physics point of view, hybrid systems that e.g. contain a single quantum dot coupled to a nanoantenna provide rich insight into light-matter-interaction at the nanoscale.[17,18] Broadband, strongly scattering nanostructures placed in the near-field of a single quantum emitter can form single photon nanoantennas, allowing for intensity and directivity control on the level of single photons.[8] The demonstration of bright, on-demand, on-chip single photon sources poses one of the major challenges in quantum optical technologies, with applications in quantum computing, encryption, communication and integrated photonic devices.[2,19] As a second application area, arrays of nanoantennas that are selectively functionalized in their hotspots play a crucial role for

a. Institute for Applied Physics and Center LISA⁺, Eberhard Karls Universität Tübingen, Auf der Morgenstelle 10, 72076 Tübingen, Germany.
   E-Mail: monika.fleischer@uni-tuebingen.de
b. The Molecular Foundry, Lawrence Berkeley National Laboratory, 1 Cyclotron Road, Building 67, Berkeley, CA94720, USA.
c. Present address: Gemological Institute of America, New York, NY 10036, USA.
d. Present address: UCSF Helen Diller Family Comprehensive Center, San Francisco, CA 94158, USA.
e. Present address: Department of Mechanical Engineering, Columbia University, New York, New York 10027, USA.

devices requiring multiplexing. E.g., nanoscale multi-colour sources are the foundation for nano-pixels in high-resolution screens.[20] Likewise, multiplexing is increasingly required in the exponentially growing field of optical sensing, including localized surface plasmon sensors, colorimetric sensing, and SERS.[21] Label-free SERS is used to identify the constituents of complex biochemical systems from their unique Raman fingerprints.[22] For efficient SERS platforms that can be applied e.g. for clinical diagnostics, safety, environmental or food monitoring, the local analyte concentration needs to be enriched in the electromagnetic hotspots, where the Raman intensity enhancement will be strongest.[23,24] To increase the integration density of the sensor elements and minimize the required volume and time, SERS-based immunoassays in microfluidic systems can be equipped for simultaneous multiplexed detection of multiple analytes by locally varying functionalization with different recognition elements.[22,25,26]

So far, a variety of techniques have been employed for the targeted positioning of nano-objects in nanoantenna hotspots. Some of these methods require prior knowledge of the hotspot location. Such high-precision techniques include the commonly used overlay electron beam lithography,[1,9] back-etching of a mask to access geometrically exposed tips,[6,27] selective functionalization,[28] partial passivation of the surface,[29-31] pushing nano-objects with a scanning probe,[4,5] or positioning nanoparticles and fluorophores by DNA origami.[32] The most promising strategy for successful coupling to hotspots is to harness the physical properties of the hotspot itself for attracting and attaching the nano-objects. A dynamic strategy for intensity maximization has been demonstrated by attaching either the nanoantenna or the emitter to a probe tip and scanning it across the immobilized complementary component.[7,33,34] The high field gradients associated with antenna near-fields have been employed for electrophoretic attraction of nano-objects,[35,36] as well as for nano-optical trapping.[37-39] High local field intensities have been exploited for attaching nano-emitters that are dispersed in a polymeric matrix by plasmon-induced, two-, or three-photon photo-polymerization.[40,20,15] These approaches however only work for emitters dispersed in a fluidic system or a polymeric matrix.

In the present approach, we introduce a self-aligned process for attaching nano-emitters in the hotspots of nanocone antennas using a dry laser ablation process. Gold nanocones have been shown to exhibit large field enhancement and strongly confined near-fields close to their tip apex when excited with electric field components polarized parallel to the cone axis.[41] The nanocones can be fabricated by different well-controlled processes that are described in detail elsewhere.[42-45] The optical properties of such nanocones have been characterized by dark-field spectroscopy and near-field optical microscopy.[10,41,46-48] Here, we apply the ablation process to attach both fluorescently marked proteins and Raman-active molecules exclusively to nanoantennas that have been exposed to the laser focus. The dose-dependent ablation is further monitored by scanning electron microscopy (SEM), photoluminescence, and dark-field spectroscopy. The three-dimensional nanocones have the geometric advantage that the hotspot is prominently located at the cone apex, which is positioned most closely to the resist surface. The exact mechanism of the self-aligned process based on local near-field effects and/or local heat generation in combination with the nanocone geometry is still to be determined.
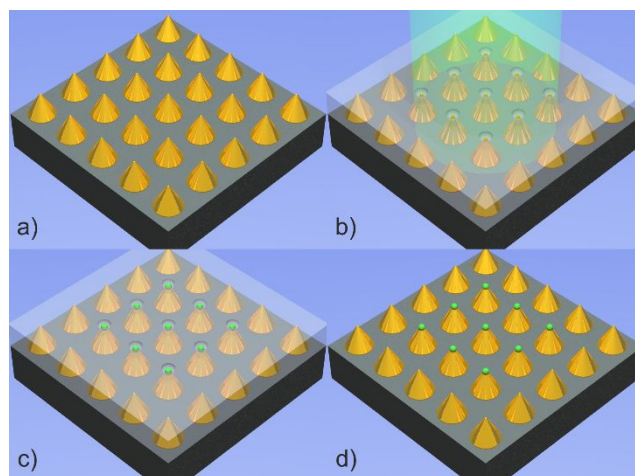

Figure 1 (a) *Gold nanocones on a substrate are (b) embedded in MAC, and the tips are laid open by laser ablation. (c) The tips are functionalized, and (d) the MAC is removed with acetone, leaving nanocones with selectively functionalized tips.*

Results and discussion

Arrays of gold nanocones with sizes on the order of 100 nm are fabricated as described in the Experimental section. The structures are embedded in a layer of 4-methylacetoxy-calix[6,8]arene (MAC). The role of the MAC is to make the nanocone tips accessible for the attachment of nano-emitters, while masking both the substrate and the base of the cones. MAC, like other calixarene derivatives, is known as a negative tone resist for electron beam lithography and can be used for high resolution patterning.[49] Recently, a dry development method demonstrating selective laser ablation of MAC that has been exposed with an electron beam was demonstrated by the authors, turning it into a positive tone process.[50,51] In the present work, the resist around the tip apex is removed by dry laser ablation as well, but here the laser illumination itself is employed as the required energy source for local patterning. Two basic mechanisms come into play: Strong local electric fields are created at the nanocone tips (and/or the base edge, depending on the polarization – see discussion in Experimental: Laser ablation) under laser illumination. The increased local intensity may be instrumental in locally changing the chemical structure of the calixarene – either directly, or through an intermediate step of plasmon-driven hot-electron generation – [52-54] in order to exceed the ablation threshold and remove the MAC from the hotspot regions in a self-aligned process.[51] At the same time, plasmonic nanoantennas exhibit high absorption cross-sections, leading to considerable heat generation at the location of the nanostructure within a laser focus,[55-57] which may induce local thermal ablation of the MAC. Resist ablation processes, as reported here and widely in literature, are typically due to non-linear two- and multi-photon processes. It was shown previously by the authors that the onset of MAC ablation following an electron beam exposure is likewise based on a two-photon process, from which the process was deduced
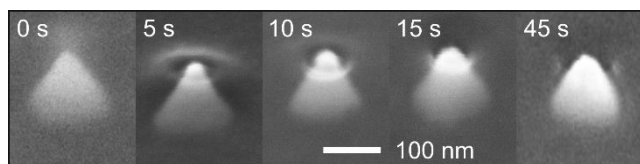
Figure 2 *SEM images (viewed under 45°) of gold nanocones embedded in MAC after different exposure times by a 35 mW HeNe laser. The ablation starts at the tip (after 5 s) and ends when a shell of MAC is removed around the nanocone (45 s).*

to be predominantly photochemical, since photothermal ablation would be a one-photon process.[50] While calixarenes are known for their relatively high thermal stability up to few 100 °C, they can be removed by thermal treatment at higher temperatures.[58] It has been shown that the threshold temperature for thermal ablation may be locally reduced by previous treatment, e.g. by electron beam lithography.[58] For the pristine MAC used in the present experiments, ablation was observed starting from ~300 °C upon heating. This value falls within the range of increased temperatures that may be induced in gold nanoparticles under laser illumination.[55-57] The fact that the shape of the nanocones remains intact under illumination as seen from Fig. 2 and the reversible spectra in Fig. 3 indicates that the temperatures remained below the nanostructure melting point. Further experiments, e.g. on planar antennas under illumination with different polarizations, will be required to determine the exact mechanism of the ablation and the respective roles of the near-field and temperature effects.

A schematic of the dry laser ablation approach can be seen in Figure 1. By spin-coating a nanocone sample (Figure 1a) with MAC resist, the nanocones are covered completely by a thin film of the MAC. Illumination of the embedded cones with a continuous wave laser leads to the dry ablation of MAC near their apices (Figure 1b). When assessing the ablation efficiency during exposure, one also needs to take the geometric configuration into account. Even if strong bond breaking occurs near the cone base, no ablation will be possible while this region is still embedded in resist. Enhanced ablation from the tip region, however, is enabled as the resist thickness is gradually reduced during the ablation process. The resulting hole size can be controlled via the laser power or exposure time (dose) and will be discussed below.

In the next step, the nano-system of choice can be applied on top of the array of nanocones, where the tips of the cones have been exposed in distinct areas (Figure 1c). In this work, two systems are presented as an indication of the self-aligned assembly of nano-emitters in the hotspots: fluorescently labeled bovine serum albumin (BSA) as a sample luminescent system, and 4-mercaptobenzoic acid (MBA) as an exemplary Raman-active system. In both approaches, the unablated MAC is removed in acetone after the functionalization (Figure 1d).

SEM images of different nanocones of the same sample embedded in MAC after different laser exposure times with a focused HeNe laser are shown in Figure 2. The process of
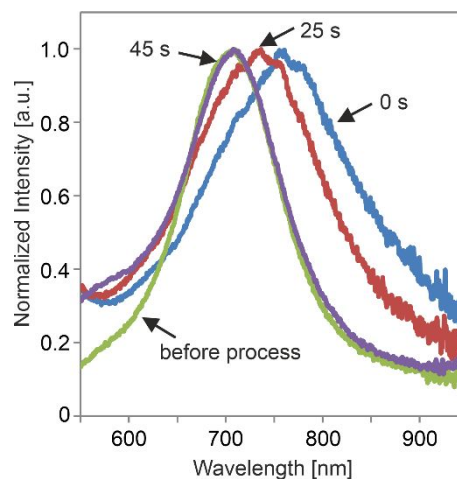

Figure 3 *Dark-field spectra of single nanocones. Green (before process): before embedding the nanocones in MAC; blue (0 s): after embedding in MAC, no exposure; red (25 s): after 25 s laser exposure; purple (45 s): after 45 s laser exposure.*

removing the MAC from the nanocones starts at the surface of the MAC layer above the cone tip, where the local field enhancement is strongest. In this case, the MAC is locally removed from the tip after 5 s. This configuration enables the attachment of a small amount of nano-emitters within the hotspot at the tip of the cone. If the cone is exposed for a longer time, more MAC is removed until the nanocone is surrounded by a thin layer of air where the MAC has been removed (Figure 2, 45 s).

To determine how much of the MAC is removed after a certain laser exposure, the process can be monitored via the scattering spectra of the nanocones themselves. It is well known that the localized plasmon resonance spectra of metal nanostructures are shifted when the refractive index of their surrounding changes.[59] The evolution of this shift with continuing exposure is now followed. The inverted microscope that is used for the ablation process (see Experimental section) is equipped with a dark-field condenser and a spectrometer, such that single particle dark-field spectra can be measured in-situ during the different steps of the ablation process. The characteristic dark-field spectra of the cones before embedding in MAC and during the different steps of the ablation are shown in Figure 3. Note that due to the detection geometry, the main peak in the spectra corresponds to an in-plane excitation of the base mode of the cones, whereas the out-of-plane mode that is responsible for the near-field enhancement at the tip apex is located at shorter wavelengths, i.e. has better overlap with the excitation laser wavelengths.[47] Embedding of the cones leads to a shift of the resonances to longer wavelengths due to the higher refractive index of MAC compared to air. Subsequent removal of the MAC by ablation leads to a continuous shift to shorter wavelengths depending on the exposure time, until all MAC directly surrounding the cone is removed, and the original resonance frequency is recovered. The fact that the spectrum after 45 s coincides with the original spectrum also indicates that the nanostructure was not damaged by the illumination
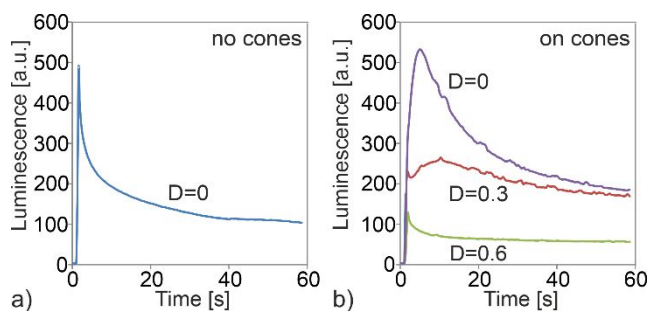
Figure 4 *Luminescence intensity measured during laser exposure of MAC over time. (a) Measured without filter (D=0) next to a cone array. (b) Purple: Measured without filter (D=0) on a cone array. Red: Measured with D=0.3 on a cone array. Green: Measured with D=0.6 on a cone array. The distinct rise of the PL after the first drop indicates the onset of the ablation process. Next to the cone array ((a), blue) and with the D=0.6 filter (green) the exposure dose remains below the ablation threshold, and no ablation takes place.*

Figure 6 *a) Raman spectrum of MBA on exposed cones (black), reference spectrum on non-exposed cones (red). b) Line scan over four functionalized areas. The background (mainly gold luminescence) was subtracted, and the maximum intensity of the Raman peak is plotted.*

process. Note that this procedure could also be used to tune the resonance frequency of the nanocones while keeping the hotspot of the structure accessible by varying the residual amount of MAC around the cone base.

As reported in Refs. 50,51, the ablation of MAC is accompanied by a characteristic luminescent behavior. By means of a Nd:YAG laser setup with a spectrometer, we therefore monitor the appearance of the luminescent species characteristic for the ablation process over the course of the laser ablation. The change of the integrated photoluminescence (PL) of the MAC over time is shown in Figure 4. Figure 4(a) shows the time evolution of the luminescence of the MAC layer without nanocones. As noted previously,[50] initially a rise in the PL signal is observed, which drops off within seconds of exposure. This initial, relatively narrow PL peak is not associated with the ablation process and may be due to the excitation and photobleaching of small molecule impurities in the MAC. In Figure 4(b), the integrated PL signal over time is shown on an array of nanocones with a lattice constant of 250 nm, measured without a neutral density (ND) filter (D=0, purple curve), as well as with ND filters of D=0.3 (50% transmittance, red curve) and D=0.6 (25% transmittance, green curve). The shapes of the D=0 and D=0.3 curves that correspond to higher laser powers show a broader luminescence peak that is indicative of the MAC ablation and coincides with a reduction of the layer thickness,
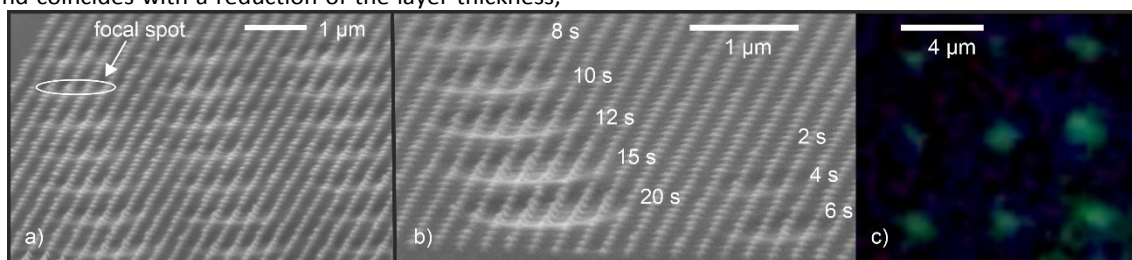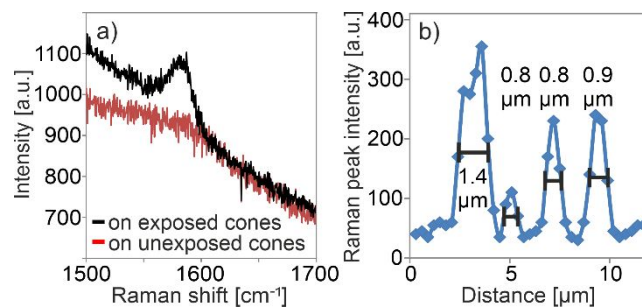
as discussed before.[50,51] At the highest power density (D=0) this broad peak appears directly, indicating the immediate creation of the luminescing species indicative of ablation. At lower power density, with D=0.3, the peak is shifted and broadened as these fluorescent species are created at lower rates. At the lowest transmittance, for D=0.6, the power density remains below the required ablation threshold, i.e. the incubation time for ablation exceeds the overall exposure time,[50] and no ablation takes place even on the nanocones. Here the PL curve has the same shape as that of the non-ablating MAC layer without nanocones (Figure 4(a)). Hence it is clear that the nanocones provide a local change, which allows the local absorption to rise above the ablation threshold.

In order to get an indication of the suitability of this ablation method for selective positioning of molecules at the cone tips, fluorescently labeled BSA is now applied to arrays of nanocones, where the surfaces of the cones are partly laid open in distinct zones. The diameter of the zones corresponds to that of the focused laser spot used for the exposure (~ 1.3 μm). The zones can be flexibly arranged within the cone array for selective functionalization. Figure 5a shows a SEM overview of an array of nanocones with uncovered tips in areas with ~1.3 μm diameter each. In Figure 5b the MAC on an array of nanocones has been exposed for different times (2 s to 20 s) by the Nd:YAG laser (ND filter D=0.3). The ablation process starts after 4 s. After about 15 s the cones are uncovered completely in the center of the focal spot. Here we also observe more slowly varying depressions in the resist that correlate with laser beam size and

Figure 5 *a) SEM image (viewed under 60°) of an array of nanocones with centre-to-centre distances of 250 nm embedded in MAC. The tips of the nanocones are laid open in the exposed areas (circles with a diameter of ~1.3 μm, indicated by the white ellipse, with a spacing of ~ 2 μm). b) Nanocones in MAC after different exposure times (D = 0.3). c) Fluorescence image showing that BSA molecules were selectively positioned in the areas with uncovered cone surfaces, where the resist was exposed in a grid with ~ 4 μm spacing. Regularly arranged fluorescent spots with ~ 1 to 1.5 μm diameter are observed.*

dose and indicate a modification of the resist around the cones, adding to the effect of resist removal at the tips. After BSA has been deposited on the sample, a lift-off process is performed in acetone, such that BSA remains only on the cones that have been accessed by the laser ablation. It has been shown in literature that several monolayers of BSA remain on the gold surface even after rinsing with acetone.[60] After the lift-off the sample is imaged in a fluorescence microscope, demonstrating that BSA is attached selectively in the exposed regions (array of focal spots with ~ 4 μm spacing, see Figure 5c). To illustrate the connection between images in Fig. 5 more clearly, additional optical microscopy images are shown in Fig. S1 in the Supplementary Information. The signal is integrated over the about 20 nanocones within the focal spot, since the diffraction limited technique does not offer sufficient spatial resolution to resolve individual cones, and the signal from a single cone would be below the detection limit. The Figure clearly shows regularly spaced localized fluorescent spots with a diameter on the order of the focus size where the BSA had access to the nanocones, with a dark background in the nanostructured, but non-exposed areas in between.

For applications in sensors or bioassays, it may be desirable to functionalize only distinct areas e.g. of a SERS substrate in order to prevent nonspecific binding events, or to enable multiplexing by applying different recognition elements to different areas across a miniaturized sensor platform. As a proof-of-principle for such spatially limited tip functionalization, MBA is now selectively attached to the tips of nanocones in distinct areas as described above. Raman measurements are performed on an array of 100 nm high nanocones with center-to-center distances of 250 nm within several hours after functionalization, using a micro-Raman setup with a focal spot diameter of ~ 1 μm (see Experimental section). The MAC mask was removed such that about 15 nm of the cone tips were accessible for the MBA molecules. Figure 6a shows a characteristic Raman peak of MBA at 1572 cm^{-1} measured on one of the functionalized sample areas. The sloping background signal originates from the gold luminescence. In a reference measurement on cones that were not exposed to the laser spot during the ablation process, accordingly no MBA signal is detected (Figure 6a). Figure 6b is the result of a line scan across four MBA-functionalized spots. The diameter of the functionalized areas is indicated by the FWHM of the measured peaks in Figure 6b and ranges between 0.8 and 1.4 μm. This measurement shows that the Raman signal is restricted to the functionalized areas, demonstrating the successful selective functionalization of the addressed cones.

Both the Raman and the fluorescent signal show fluctuations between the different focal spots. This can be attributed to a combination of the inherent nanoscale variations of the nanofabrication process leading to small deviations in the cone geometry, and thus in the near-field enhancement as well as the ablation; to the fact that the signal intensity is integrated over a double-digit number of cones within each focal spot; and to the statistical binding process of the molecules from solution. In future work, individual nanocones might be functionalized with few molecules in self-assembled monolayers and investigated by techniques allowing for single-molecule sensitivity beyond the diffraction limit to gain single-particle information.

Experimental

Nanostructure fabrication

Arrays of gold nanocones are prepared both on silicon and on indium tin oxide coated glass slides that are covered by a gold layer and spin-coated with a layer of PMMA. The gold layer sputtered onto the substrates determines the height of the nanocones. Here, nanocones with nominal heights of 70 nm and 100 nm are prepared. Electron beam lithography (Philips XL30, 30 kV) is used to expose nanoholes in the PMMA, followed by the evaporation of aluminum oxide (20 nm for the 70 nm cones and 25 nm for the 100 nm cones), which results in aluminum oxide dots after a lift-off in acetone. By using these dots as an etch mask, solid gold nanocones are formed by argon ion milling (acceleration voltage: 300 V) of the gold layer.[10,42,43]

Nanostructure embedding

MAC is dissolved in MIBK (methyl isobutyl ketone) with a concentration of 4%. Afterwards the solution is filtered in order to remove larger agglomerates. Alternatively, a solution of MAC in chlorobenzene can be used. Spin-coating the MAC with a speed of 2000 rpm leads to a layer of 80 nm thickness, which is sufficient to cover nanocones of 70 nm height. For different cone heights the dilution of the solution or the spin-coating parameters can be easily adjusted.

Laser ablation

For the ablation process two setups were used. A Horiba micro-Raman setup with a 12 mW frequency doubled continuous wave Nd:YAG laser at a wavelength of 532 nm that is focused by a 50x objective with a numerical aperture (NA) of 0.5. The focal spot has a diameter of ~ 1 μm, which leads to a power density of ~ 1.5 MW/cm^2 on the sample without ND-Filter. In the second setup a HeNe laser with a power of 35 mW (wavelength 632.8 nm) is used that is coupled into an inverted Nikon Ti microscope and focused by a 60x objective with a NA of 0.7, which leads to a focal spot of ~ 1.3 μm in diameter. The microscope is additionally equipped with a dark-field condenser (NA=0.8-0.95) and a spectrometer (Princeton Instruments Acton Spectra Pro 2300i) for dark-field spectroscopy. In both cases the sample with the nanocones in MAC is mounted to a microscope scanning stage and illuminated from above.

Depending on the orientation of the electric field components of the incident electromagnetic field, different plasmonic modes can be excited in the nanocones. While electric fields polarized parallel to the cone base create an enhanced near-field around the base edge of the nanocone, electric field components parallel to the cone axis create a strong, highly localized near-field at the cone apex.[47,48] Due to the tight focusing of the linearly polarized laser beams in the configurations above, electric field components in all spatial directions (E_x, E_y, E_z) are present in the focal spot.[45,61,62] Whereas the in-plane field component corresponding to the original linear polarization contributes most strongly, the axial component leads to the relatively strongest near-field enhancement. It is therefore to be expected that near-field enhancement is excited both at the tip and the base edge of the nanocones (see also Figure S2 in the

Supplementary Information). Further studies are required to clarify whether the ablation process depends mostly on near-field effects, thermal effects, or a combination of both. Either way the geometry of the nanocone favors ablation at the cone tip, since the material can be directly removed from the surface, while ablation from lower parts is blocked by the material above. A polarization-dependent study for the cone geometry might be performed by illumination with tightly focused cylindrical vector beams,[10,63,64] while the near-field enhancement at the tip under perpendicular incidence could be further increased by tilting the nanocone axes.[64]

Tip functionalization

To functionalize the cone tips, in the first approach fluorescently labeled bovine serum albumin (BSA) in an aqueous solution is spin-coated or drop dried on samples with arrays of nanocones where the tips of the cones have been exposed in distinct areas. In the second example, the cone tips in distinct areas of a sample are laid open by laser ablation, and 4-mercaptobenzoic acid (MBA) is chemically attached to the gold tips. MBA molecules are chosen because their thiol groups form a strong bond with the gold, and MBA exhibits a strong Raman signal intensity, which is required for detecting the low amounts of molecules attached to the cone tips. After laying open the cone tips with the process described above, a 10 s oxygen reactive ion etching treatment is performed on the sample in order to remove possible impurities from the gold tips. Such a treatment does not affect the shape of the gold structure, but may improve the assembly of molecules by thiol chemistry on gold surfaces.[65] The MAC mask covering the sample is etched back by less than 5 nm (measured by a Dektak surface profiler) in the process. Then the sample is incubated in an aqueous solution of MBA for about 20 h in ambient conditions. In both approaches, the MAC is removed in acetone followed by rinsing the sample with deionized water and ultrasonication.

Raman spectroscopy

Raman measurements were performed within several hours after functionalization, using a micro-Raman setup with a 100x objective (NA 0.9). For these measurements an 18 mW HeNe laser at 632.8 nm and a D=1 grey filter are used to reduce the laser power in order to prevent damaging the molecules. The measurement was performed on an array of 100 nm high nanocones with center-to-center distances of 250 nm, corresponding to ~ 12 nanocones positioned within the focal spot (diameter ~ 1 μm) during the exposure.

Conclusions

In conclusion it was shown that the tips of metallic nanocones acting as optical antennas can be locally uncovered by dry laser ablation of MAC resist, while the remaining sample including the cone bases remains embedded. The ablation threshold is locally exceeded by the high electric near-field within the hotspots, the local heat generation by the nanoantennas, or the interplay of both. This technique is of interest for the positioning of nanoemitters and selective functionalization of the hotspots at the cone tips. Fluorescently labeled BSA

molecules are positioned on the cones within the ablated areas and detected by fluorescence microscopy. For selective Raman imaging the gold nanocones are functionalized with MBA molecules in distinct areas within an array of cones. The size of these areas exhibiting functionalization corresponds to the diffraction limited resolution of the laser focus. Since SEM images demonstrate that before functionalization the cones are embedded by MAC except for the accessible cone tips, and since no signal is observed from cones that were fully embedded by MAC, the functionalized individual spots within these areas are expected to coincide with the nanoscale spots of high electromagnetic field intensity at the excited cone tips. The attached MBA molecules are detected by surface enhanced Raman spectroscopy at the exposed positions only.

The origin of the ablation process needs to be further investigated, e.g. by using planar structures and polarization-dependent studies. Based on the dry laser ablation technique, a variety of different hybrid nanostructures could be created. If mostly driven by local heat generation, it may be used to selectively access the surfaces of planar nanoantennas while masking the substrate. If predominantly based on near-field effects, it might offer a general strategy for accessing the near-surface hotspots of arbitrarily shaped nanoantennas for self-aligned attachment. Selective functionalization strategies are of vital interest for application areas that require coupling and energy transfer between specific antennas and emitters, e.g. in single photon sources for quantum nanophotonics, or multiplexing for high-throughput parallel biosensing.

Conflicts of interest
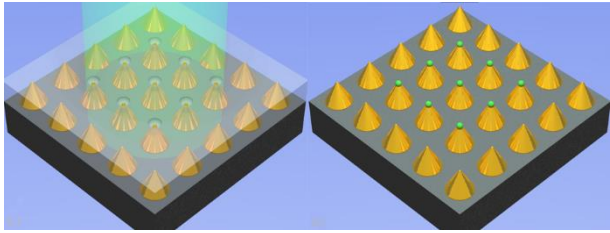
There are no conflicts to declare.

Acknowledgements

References

1 A.G. Curto, G. Volpe, T.H. Taminiau, M.P. Kreuzer, R. Quidant and N.F. van Hulst, *Science*, 2010, **329**, 930.
2 N. Livneh, M.G. Harats, D. Istrati, H.S. Eisenberg and R. Rapaport, *Nano Lett.*, 2016, **16**, 2527.
3 L. Xin, M. Lu, S. Both, M. Pfeiffer, M.J. Urban, C. Zhou, H. Yan, T. Weiss, N. Liu and K. Lindfors, *ACS Photonics*, 2019, **6**, 985.
4 M. Pfeiffer, K. Lindfors, C. Wolpert, P. Atkinson, M. Benyoucef, A. Rastelli, O.G. Schmidt, H. Giessen and M. Lippitz, *Nano Lett.*, 2010, **10**, 4555.
5 A.W. Schell, G. Kewes, T. Hanke, A. Leitenstorfer, R.

Bratschitsch, O. Benson and T. Aichele, *Opt. Express*, 2011, **19**, 7914.

6 A.J. Meixner, R. Jäger, S. Jäger, A. Bräuer, K. Scherzinger, J. Fulmes, S. zur Oven Krockhaus, D.A. Gollmer, D.P. Kern and M. Fleischer, *Faraday Discuss.*, 2015, **184**, 321.

7 K. Matsuzaki, S. Vassant, H.-W. Liu, A. Dutschke, B. Hoffmann, X. Chen, S. Christiansen, M.R. Buck, J.A. Hollingsworth, S. Götzinger and V. Sandoghdar, *Sci. Rep.*, 2017, **7**, 42307.

8 A.F. Koenderink, *ACS Photonics*, 2017, **4**, 710.

9 B. Metzger, M. Hentschel, T. Schumacher, M. Lippitz, X. Ye, C.B. Murray, B. Knabe, K. Buse and H. Giessen, *Nano Lett.*, 2014, **14**, 2867.

10 P. Reichenbach, A. Horneber, D.A. Gollmer, A. Hille, J. Mihaljevic, C. Schäfer, D.P. Kern, A.J. Meixner, D. Zhang, M. Fleischer and L.M. Eng, *Opt. Express*, 2014, 22, 15484.

11 T.W. Johnson, Z.J. Lapin, R. Beams, N.C. Lindquist, S.G. Rodrigo, L. Novotny and S.-H. Oh, *ACS Nano*, 2012, **6**, 9168.

12 K. Kneipp, Y. Wang, H. Kneipp, L.T. Perelman, I. Itzkan, R.R. Dasari and M.S. Feld, *Phys. Rev. Lett.*, 1997, **78**, 1667.

13 K. Kneipp, H. Kneipp, I. Itzkan, R.R. Dasari and M.S. Feld, *J. Phys.: Condens. Matter*, 2002, **14**, R597.

14 D.A. Stuart, C.R. Yonzon, X. Zhang, O. Lyandres, N.C. Shah, M.R. Glucksberg, J.T. Walsh and R.P. Van Duyne, *Anal. Chem.*, 2005, **77**, 4013.

15 C.M. Galloway, M.P. Kreuzer, S.S. Aćimović, G. Volpe, M. Correia, S.B. Petersen, M.T. Neves-Petersen and R. Quidant, *Nano Lett.,* 2013, **13**, 4299.

16 W. Bao, A.S. McLeod, S. Cabrini, J.B. Neaton and P.J. Schuck, *J. Opt.,* 2014, **16,** 114014.

17 M.J. Achermann, *J. Phys. Chem. Lett.*, 2010, **1**, 2837.

18 S.A. Maier and H.A. Atwater, *J. App. Phys.*, 2005, **98**, 011101.

19 Y. Sun, V. Yaroshenko, A. Chebykin, E. Ageev, S. Makarov and D. Zuev, *Opt. Mater. Express*, 2020, **10**, 29.

20 X. Zhou, J. Wenger, F.N. Viscomi, L. Le Cunff, J. Béal, S. Kochtcheev, X. Yang, G.P. Wiederrecht, G. Colas des Francs, A.S. Bisht, S. Jradi, R. Caputo, H.V. Demir, R.D. Schaller, J. Plain, A. Vial, X.W. Sun and R. Bachelot, *Nano Lett.*, 2015, **15**, 7458.

21 Z. Li, L. Leustean, F. lnci, M. Zhenga, U. Demirci and S. Wang, *Biotechnol. Adv.*, 2019, **37**, 107440.

22 N. Kim, M.R. Thomas, M.S. Bergholt, I.J. Pence, H. Seong, P. Charchar, N. Todorova, A. Nagelkerke, A. Belessiotis-Richards, D.J. Payne, A. Gelmi, I. Yarovsky and M.M. Stevens, *Nat. Commun.*, 2020, **11**, 207.

23 M.L. Mekonnen, C.-H. Chen, W.-N. Su, B.-J. Hwang, *Microchem. J.*, 2018, **142**, 305.

24 H.K. Lee, Y.H. Lee, C.S. Lin Koh, G.C. Phan-Quang, X. Han, C.L. Lay, H.Y.F. Sim, Y.-C. Kao, Q. An and X.Y. Ling, *Chem. Soc. Rev.*, 2019, **48**, 731.

25 A. Kamińska, K. Winkler, A. Kowalska, E. Witkowska, T. Szymborski, A. Janeczek and J. Waluk, *Sci. Rep.*, 2017, **7**, 10656.

26 Z. Wang, S. Zong, L. Wu, D. Zhu and Y. Cui, *Chem. Rev.*, 2017, **117**, 7910.

27 J. Fulmes, R. Jäger, A. Bräuer, C. Schäfer, S. Jäger, D.A. Gollmer, A. Horrer, E. Nadler, T. Chassé, D. Zhang, A.J. Meixner, D.P. Kern and M. Fleischer, *Nanoscale*, 2015, **7**, 14691.

28 A.L. Lereu, J.P. Hoogenboom and N.F. Van Hulst, *International Journal of Optics*, 2012, **2012**.

29 J.Y. Chang, H. Wu, H. Chen, Y.C. Ling and W. Tan, *Chem. Commun.*, 2005, 1092.

30 P. Zijlstra, P.M. R. Paulo and M. Orrit, *Nat. Nanotechnol.*, 2012, **7**, 379.

31 W.M. Park, B.G. Choi, Y.S. Huh, W.H. Hong, S.Y. Lee and T.J. Park, *ChemPlusChem*, 2013, **78**, 48.

32 A. Puchkova, C. Vietz, E. Pibiri, B. Wünsch, M. Sanz Paz, G.P. Acuna and P. Tinnefeld, *Nano Lett.*, 2015, **15**, 8354.

33 J. N. Farahani, D.W. Pohl, H.-J. Eisler and B. Hecht, *Phys. Rev. Lett.*, 2005, **95**, 017402.

34 H Eghlidi, K.G. Lee, X.W. Chen, S. Götzinger, and V. Sandoghdar, *Nano Lett.* 2009, **9**, 4007.

35 C. Schäfer, D.P. Kern and M. Fleischer, *Lab Chip*, 2015, **15**, 1066.

36 A. Barik, S. Cherukulappurath, N.J. Wittenberg, T.W. Johnson and S.-H. Oh, *Anal. Chem.*, 2016, **88**, 1704.

37 M. L. Juan, M. Righini and R. Quidant, *Nat. Photon.,* 2011, **5** 349.

38 A. A. Al Balushi, A. Kotnala, S. Wheaton, R. M. Gelfand, Y. Rajashekara and R. Gordon, *Analyst*, 2015, **140,** 4760.

39 R. A. Jensen, I-C.Huang, O. Chen, J. T. Choy, T. S. Bischof, M. Lončar and M. G. Bawendi, *ACS Photonics*, 2016, **3**, 423.

40 X. Zhou, C. Deeb, S. Kostcheev, G.P. Wiederrecht, P.-M. Adam, J. Béal, Jérôme Plain, D.J. Gosztola, J. Grand, N. Félidj, H. Wang, A. Vial and R. Bachelot, *ACS Photonics*, 2015, **2**, 121.

41 M. Fleischer, C. Stanciu, F. Stade, J. Stadler, K. Braun, A. Heeren, M. Häffner, D.P. Kern and A.J. Meixner, *Appl. Phys. Lett.*, 2008, **93**, 111114.

42 F. Stade, A. Heeren, M. Fleischer and D.P. Kern, *Microelectron. Eng.*, 2007, **84**, 1589.

43 M. Fleischer, F. Stade, A. Heeren, M. Häffner, K. Braun, C. Stanciu, R. Ehlich, J.K.H. Hörber, A.J. Meixner and D.P. Kern, *Microelectron. Eng.*, 2009, **86**, 1219.

44 M. Fleischer, A. Weber-Bargioni, M.V.P. Altoe, A.M. Schwartzberg, P.J. Schuck, S. Cabrini and D.P. Kern, *ACS Nano*, 2011, **5**, 2570.

45 A. Horrer, C. Schäfer, D.A. Gollmer, K. Broch, J. Rogalski, J. Fulmes, D. Zhang, A.J. Meixner, F. Schreiber, D.P. Kern and M. Fleischer, *Small*, 2013, **9**, 3987.

46 G. Bautista, M.J. Huttunen, J. Mäkitalo, J.M. Kontio, J. Simonen and M. Kauranen, *Nano Lett.*, 2012, **12**, 3207.

47 C. Schäfer, D.A. Gollmer, A. Horrer, J. Fulmes, A. Weber-Bargioni, S. Cabrini, P.J. Schuck, D.P. Kern and M. Fleischer, *Nanoscale*, 2013, **5**, 7861.

48 J. Fulmes, C. Schäfer, D.P. Kern, P.-M. Adam and M. Fleischer, *Nanotechnology*, 2019,**30**, 415201.

49 H. Sailer, A. Ruderisch, D. P. Kern and V. Schurig, *J. Vac. Sci. Technol. B*, 2002, **20**, 2958.

50 D.G. Oteyza, P.N. Perera, M. Schmidt, M. Falch, S.D. Dhuey, B.D. Harteneck, A.M. Schwartzberg, P.J. Schuck, S. Cabrini and D.L. Olynick, *Nanotechnology*, 2012, **23**, 185301.

51 P.N. Perera, A.M. Schwartzberg, D.G. de Oteyza, S.D. Dhuey, B.D. Harteneck, S. Cabrini and D.L. Olynick, *J. Vac. Sci. Technol. B*, 2012, **30**, 06FI02.

52 A. Giugni, B. Torre, A. Toma, M. Francardi, M. Malerba, A. Alabastri, R. Proietti Zaccaria, M.I. Stockman and E. di Fabrizio, *Nat. Nanotechnol.*, 2013, **8**, 845.

53 P.J. Schuck, *Nat. Nanotechnol.*, 2013, **8**, 799.

54 Y. Zhang, S. He, W. Guo, Y. Hu, J. Huang, J.R. Mulcahy and W.D. Wei, *Chem. Rev.* 2018, **118**, 2927.

55 A. O. Govorov and H. H. Richardson, *Nano Today*, 2007, **2**(1), 30-38.

56 M. Caldarola, P. Albella, E. Cortés, M. Rahmani, T. Roschuk, G. Grinblat, R. F. Oulton, A. V. Bragas and S. A. Maier, *Nat. Commun.*, 2015, **6**, 7915.

57 X. Xie and D. G. Cahill, *Appl. Phys. Lett.*, 2016, **109**, 183104.

58 V. Auzelyte, A. Langner and H.H. Solak, *J. Vac. Sci. Technol. B*, 2009, **27**, 2990.

59 J.J. Mock, D.R. Smith and S. Schultz, *Nano Lett.*, 2003, **3**, 485.H. Ron, H. Cohen, S. Matlis, M. Rappaport and I. Rubinstein, *J. Phys. Chem. B*, 1998, **102**, 9861.

60 F. Kratz, S. Grass, N. Umanskaya, C. Scheibe, C. Müller-Renno, N. Davoudi, M. Hannig and C. Ziegler, *Colloids and Surfaces B: Biointerfaces*, 2015, **128**, 28.

61 B. Richards and E. Wolf, *Proc. Roy. Soc. A*, 1959, **253**, 358.

62 M. A. Lieb and A. J. Meixner, *Opt. Express*, 2001, **8**(7), 458.

63 M. Fleischer, D. Zhang, K. Braun, S. Jäger, R. Ehlich, M. Häffner, C. Stanciu, J. K. H. Hörber, A. J. Meixner and D. P. Kern, *Nanotechnol.*, 2010, **21**, 065301.

64 C. Dreser, D. A. Gollmer, G. Bautista, X. Zang, D. P. Kern, M. Kauranen and M. Fleischer, *Nanoscale*, 2019, **11**, 5429.

65 H. Ron, H. Cohen, S. Matlis, M. Rappaport and I. Rubinstein, *J. Phys. Chem. B*, 1998, **102**, 9861.

Table of contents entry